npj | Quantum Materials

www.nature.com/npjquantmats

ARTICLE OPEN

High-performance HgCdTe avalanche photodetector enabled with suppression of band-to-band tunneling effect in mid-wavelength infrared

Jin Chen[1,2,3], Jian Chen[1,3,4], Xin Li[1,3,4], Jiale He[1,2], Liao Yang[1,3], Jian Wang[1], Feilong Yu[1,3], Zengyue Zhao[1,3], Chuan Shen[1,3], Huijun Guo[1,3], Guanhai Li[1,2,3,5✉], Xiaoshuang Chen[1,2,3,5] and Wei Lu[1,2,3,5]

HgCdTe avalanche photodiodes promise various fascinating applications due to the outstanding capability of detecting weak signals or even single photon. However, the underlying transport mechanisms of diverse dark current components are still unresolved at high reverse bias, thus limiting the development of high-performance devices. Here, we establish an accurate model to demonstrate the competitive mechanism between band-to-band and avalanche dark currents in positive-intrinsic-negative structures. Based on the high consistency between the simulated and measured results, we find that both components jointly dominate overall dark current but with a larger avalanche current. This breaks the conventional cognition that band-to-band dark current contributes the majority. With the guidance, we reconstruct an optimized device and achieve gain 1876 (6153) and dark current 10^{-10} (10^{-9}) A at bias −10 (−10.5) V, respectively. Comparisons of dark current and gain with reported single-element devices further confirm the outstanding performance of our device.

npj Quantum Materials (2021)6:103 ; https://doi.org/10.1038/s41535-021-00409-3

INTRODUCTION

Mid-wavelength infrared (MWIR), one of three transparent atmospheric windows, has a unique advantage in full-time and all-weather space-to-ground communication applications due to its excellent capacities of small attenuation, broad bandwidth, and strong anti-interference from the background radiation of sun[1,2]. Besides, various characteristic spectra of molecules locate around the MWIR regime. Therefore, the effective and sensitive detection of MWIR photons plays a crucial role in remote sensing, national defense, and other areas[3–6]. HgCdTe-based avalanche photodetectors (APDs) are the most promising detection candidate due to the outstanding merits in the tunable bandgap, high sensitivity, low power consumption, small size, and light weight[7,8]. Compared with complex configurations like separate absorption multiplication[9] or n-Barrier-n[10] in the detection of ultra-weak[11–13] or even single photon[14–16], positive-intrinsic-negative (PIN) structure has proved its outstanding merits in aspects of easy fabrication, high reproducibility, and excellent flexibility in manufacturing focal plane array[3,17–21]. With its great potentials, PIN HgCdTe APD has attracted much attention and found various applications, such as three-dimensional laser radar and deep space detection.

Dark current and gain are a set of key indicators that always need trade-offs in practical implementations of APDs[19,22]. Researchers have proposed various mechanisms and configurations to enhance the gain and suppress the overall dark current. For instance, Kopytko et al. successfully managed the unfavorable tunneling process by controlling the doping concentration of multiplication layer[23]. Li et al. utilized the guard ring structure to break the surface local electric field to prevent the edge pre-breakdown effect and reduce the excess noise factor[24]. Besides, Singh et al. manufactured an MWIR APD with high gain based on band-to-band tunneling (BBT) mechanism at high bias[25]. However, current HgCdTe APDs always operate at linear mode, in which larger bias voltage always indicates high gain while dark current would also inevitably increase. At high bias, especially approaching breakdown point, the underlying physics that governs diverse contributing dark current components is still unclear, especially the competition between the BBT and avalanche currents, which results in the obvious deviations between the simulations and experiments and thus limiting the realization of extreme-performance single-photon avalanche detectors.

In this paper, we establish an accurate model to clarify the underlying current mechanisms of PIN HgCdTe APDs. With the excellent agreement between measured and simulated results, we explicitly demonstrate the competition between the BBT and avalanche currents and reconstruct a structure with optimized thickness and concentrations. Voltage amplification measurement is also built to characterize the blackbody responsivity and photocurrent of the designed detector at high bias. Finally, we compare the gain and dark current with the reported ones to further illustrate the superiorities of our device and confirm the flexibility and validity of our model to achieve high-performance photodetectors. Our work provides a route towards achieving perfect optoelectronic devices and may find various applications in the relatively immature but very promising MWIR regime.

RESULTS

Energy band structure and dark current analysis

Three-dimensional and cross-section views of the planar PIN APD are shown in Fig. 1a, b, respectively. The device is designed to operate in MWIR based on $Hg_{1-x}Cd_xTe$ material. Cd component

[1]State Key Laboratory of Infrared Physics, Shanghai Institute of Technical Physics, Chinese Academy of Sciences, 500 Yu-Tian Road, Shanghai 200083, China. [2]Hangzhou Institute for Advanced Study, University of Chinese Academy of Sciences, No.1 Sub-Lane Xiangshan, Hangzhou 310024, China. [3]University of Chinese Academy of Science, No. 19A Yuquan Road, Beijing 100049, China. [4]School of Physical Science and Technology, ShanghaiTech University, Shanghai 201210, China. [5]Shanghai Research Center for Quantum Sciences, 99 Xiupu Road, Shanghai 201315, China. ✉email: ghli0120@mail.sitp.ac.cn

Published in partnership with Nanjing University

npj nature partner journals

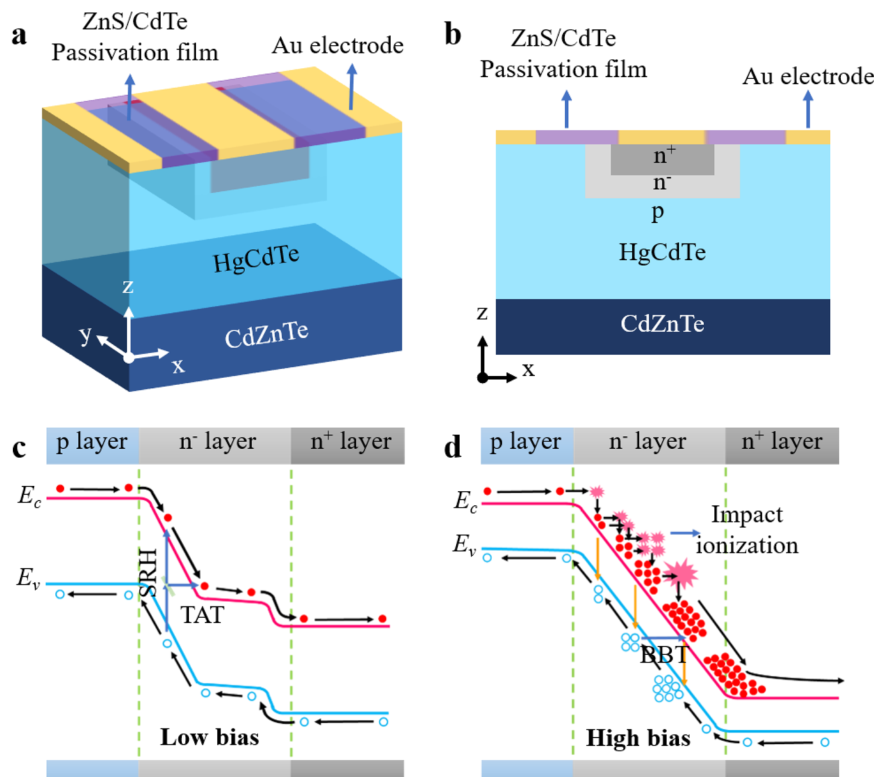

Fig. 1 Schematic of the avalanche photodetector and energy band structure. **a** Three-dimensional view and **b** cross-section view of the HgCdTe photodetector. The band structures at **c** low bias and **d** high reverse bias are shown, respectively.

fraction is 0.3. The device simulations are conducted with commercial software-Sentaurus technology computer-aided design. Different physical models of the currents are adopted to perform the simulation. Details can be found in the "Methods" section.

We start with the analysis of the energy bandstructure of conventional planar PIN HgCeTe APD. Without any bias, the interdiffusion of electron and hole emerge at the interface of pn^- junction and lead to the bending of energy band and form a potential difference, i.e., the built-in electric field. For the interface at n^-n^+ junction, the difference of doping concentration also results in the energy difference and we define the electric field here as the initial electric field. Once applying a reverse bias, the potential difference between n^- layer and p layer increases. At low bias, the n^- layer is not fully depleted. The built-in electric field and the initial electric field both exist as shown in Fig. 1c. However, at high voltage, the potential difference further increases, and the build-in electric field would overlap the initial electric field until the width of the depletion region is approximately the same as the thickness of n^- layer, which is shown in Fig. 1d. The carriers' multiplication occurs as the width of the depletion region is greater than the mean free path between the two ionizing impacts, hence leading to the avalanche effect.

In order to achieve a high-performance avalanche structure in Fig. 1a, the simulation results from the developed accurate model are compared with the experiments to validate the model in predicting the current behaviors. As shown in Fig. 2a, solid lines and triangle points which respectively represent simulated and measured results of dark current and photocurrent agree well with each other, revealing the availability to simulate the real device. The doping concentration and thickness of n^- layer are 5×10^{14} cm^{-3} and $2\,\mu m$ in simulation, which is consistent with the measured result. High consistency between simulated and measured results indicates the accuracy of the proposed model. Based on our model, the current components as a function of the bias voltage are illustrated in Fig. 2b. It can be seen that Shockley–Read–Hall (SRH) and TAT currents are the main mechanism before the threshold voltage, which is defined as the voltage where avalanche multiplication current is larger than SRH recombination. It's worth mentioning that BBT and avalanche effect dominates the current transport after threshold voltage. However, the avalanche effect is greater than the BBT effect, which is in contradiction with the conventional structures. The abnormally large avalanche current with low doping concentration $5 \times 10^{14}\,cm^{-3}$ originates from two aspects. The minority carriers-electrons that are drifted to n^+ region under reverse bias transport through the multiplication layer and form avalanche current. For n^- layer with low doping concentration, electric field intensities around pn^- and n^-n^+ junction are comparable. For certain concentrations, the electric field of n^-n^+ junction is even larger than that of pn^- junction. With external bias, both electric fields at the interfaces contribute to the avalanche multiplication. Besides, electrons tunneling from the valance band to the conductive band also participate in the avalanche process and enhance the avalanche current. It is also worth mentioning that low doping concentration would lead to the widening of effective bandgap and do benefit to the suppression of the tunneling electrons. A thorough investigation of the competitive mechanism between avalanche and BBT dark current under high bias plays a key role in the realization of high-performance HgCdTe APDs. Besides, Auger and radiative recombination have less effect on total dark current due to their strong temperature dependence.

Since the n^- layer is the multiplication layer of the avalanche detector, its geometry and doping play a key role in the device performance at different biases. Figure 2c shows the *I–V* characteristics with various doping concentrations. It can be seen that the doping concentration of $5 \times 10^{14}\,cm^{-3}$ has the lowest overall dark current among the range from 1×10^{14} to 1×10^{16} cm^{-3} under high bias. The phenomenon that the dark current level is lower than those with concentrations of 1×10^{14} and

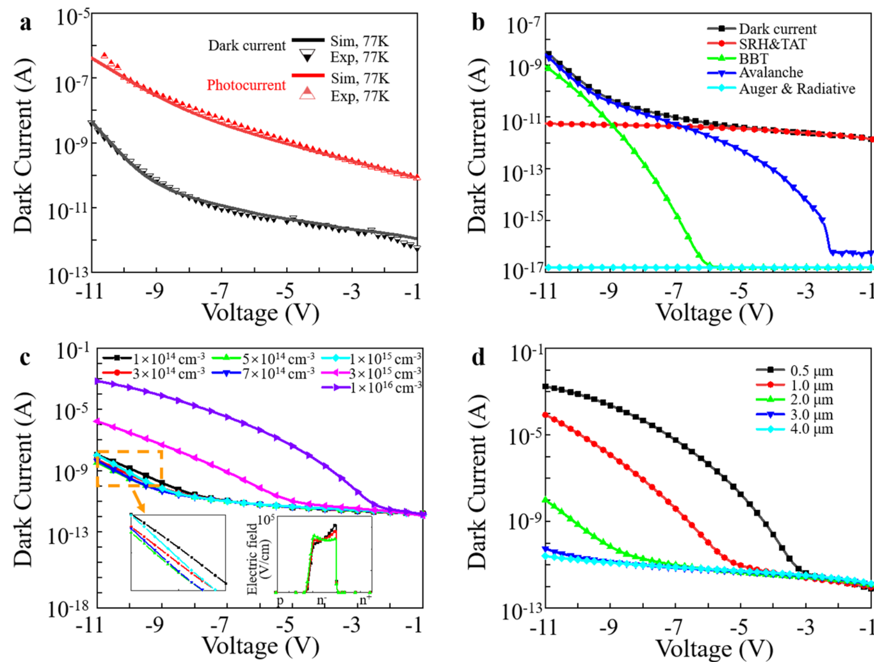

Fig. 2 The accurate model in analyzing the dark current. a Simulated and measured results of dark current and photocurrent. **b** Total dark current and dominant components for HgCdTe APD. **c** Simulated *I–V* curves with various doping concentrations of n^- layer. Insets show IV curves at high bias and the electric field for different doping concentrations at −11 V, respectively. **d** Simulated dark current as a function of voltages with different n^- layer thicknesses.

$1\times10^{15}\,\mathrm{cm}^{-3}$ can be attributed to the fact that the dark current is dominated by avalanche current under high bias and the electric field determines the avalanche multiplication. The dark current with a doping concentration of $5\times10^{14}\,\mathrm{cm}^{-3}$ at high bias is the lowest. Simulation results of other doping concentrations can be found in Supplementary Note 1. In order to illustrate this, the electric field is plotted in the inset of Fig. 2c. It can be seen that the electric field of the doping concentration $1\times10^{14}\,\mathrm{cm}^{-3}$ is larger than those of 5×10^{14} and $1\times10^{15}\,\mathrm{cm}^{-3}$. Besides, the current of the doping concentration of $1\times10^{15}\,\mathrm{cm}^{-3}$ is larger than that of $5\times10^{14}\,\mathrm{cm}^{-3}$ due to the joint contributions of the electric field at pn^- and n^-n^+ interfaces. Doping concentration also imposes a significant effect on the BBT effect and the enhancement of BBT effect dominates the dramatic increase of dark current. Besides, the excessive doping concentrations result in the junction area moving to p layer, thereby invalidating the function of n^- layer. We also investigate the current dependence on the thickness of n^- layer through simulating the *I–V* curves as shown in Fig. 2d. The dominating transport mechanisms of dark current mainly depend on the doping carriers' concentration. The SRH and TAT dark current dominate the dark current at low bias, while BBT and avalanche components occupy the majority at high bias. However, the dominating dark current components are not changed with a thickness of n^- layer. The n^- layer acts as a depletion area and its thickness is directly related to the built electric field distributions. With this consideration, the threshold voltage increases with the thickness as shown in Fig. 2d. It is also worth noting that the thickness of n^- layer also affects the quantum efficiency and response time. Therefore, an appropriate thickness is a key to achieving high-performance devices.

Figure 3a exhibits the electric field with various doping concentrations as a function of the reverse bias. The electric field increases as the reverse bias increases and gradually saturates at a high bias. Similarly, the generations of BBT and impact ionization with various doping concentrations as a function of bias are illustrated in Fig. 3b, c, respectively. Notably, the BBT generation is more sensitive to the doping concentration compared with that of impact ionization due to the fact that higher doping concentration results in the narrower effective bandgap and the increase of BBT generation is more significant than that of impact ionization as the voltage increases. The doping concentration determines the critical voltage at which the BBT generation takes effect in the device, which is in consistent with the discussion above. The BBT current is the main reason for the increase of dark current in the detector with a high doping concentration in n^- layer. However, for impact ionization, the saturation with reverse bias is more obvious as shown in Fig. 3c. Afterward, the impact ionization generation of the doping concentration of $1\times10^{14}\,\mathrm{cm}^{-3}$ is higher than that of $1\times10^{15}\,\mathrm{cm}^{-3}$. The impact ionization with different doping concentrations agrees well with the above discussion for dark current. In order to have a direct evaluation and further clarify the influence of the doping concentration of n^- layer on the device performance, the electric field, BBT and impact ionization generations as a function of doping concentration at −11 V are plotted in Fig. 3d. The electric field, BBT, and impact ionization generations are proportional to doping concentration as the doping concentration is above $1\times10^{15}\,\mathrm{cm}^{-3}$. It is should be noted that the impact of ionization generation is larger than BBT generation. For doping concentration below $1\times10^{15}\,\mathrm{cm}^{-3}$, both the BBT and impact ionization generations decrease as the doping concentration increases. However, the difference between BBT and impact ionization generation increases with the doping concentration. For doping concentration above $1\times10^{15}\,\mathrm{cm}^{-3}$, the BBT and impact ionization increase with the doping concentration but the difference between them is almost unchanged. As discussed above, the dominating mechanisms under high bias voltage are the joint BBT and avalanche ionization effects and the excessive doping concentration would cause an excessive dark current. Therefore, the doping concentration of n^- layer needs to be strictly controlled below $1\times10^{15}\,\mathrm{cm}^{-3}$ in the device fabrication.

Realization of high-performance HgCdTe APD

According to the optimized structural parameters, avalanche photodiodes are manufactured. The fabrication process is shown

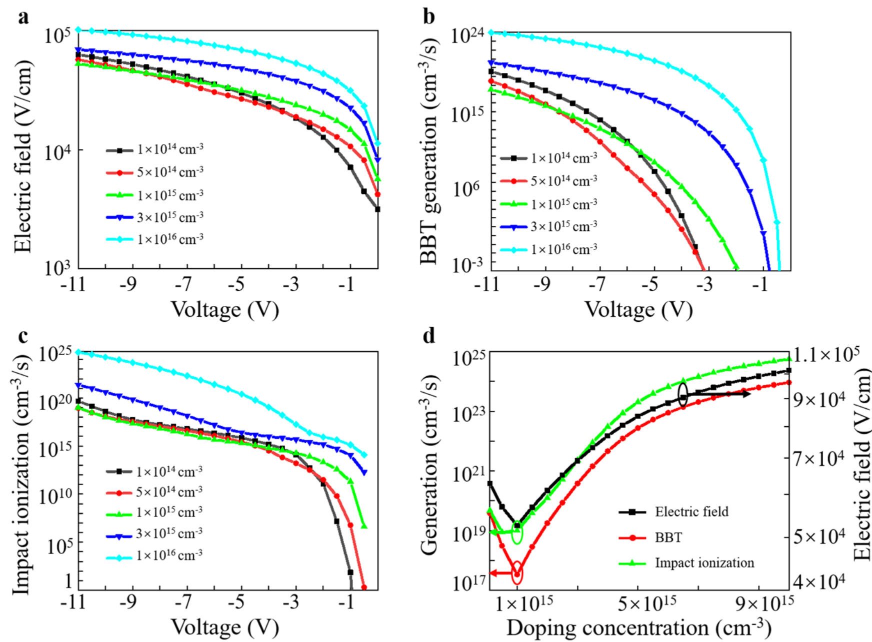

Fig. 3 Doping concentrations influence the electric field and BBT, impact ionization generations. **a** Electric field, **b** BBT generation, and **c** impact ionization generation with various doping concentrations at different bias voltages. **d** Electric field, BBT, and impact ionization generations as a function of doping concentration at −11 V.

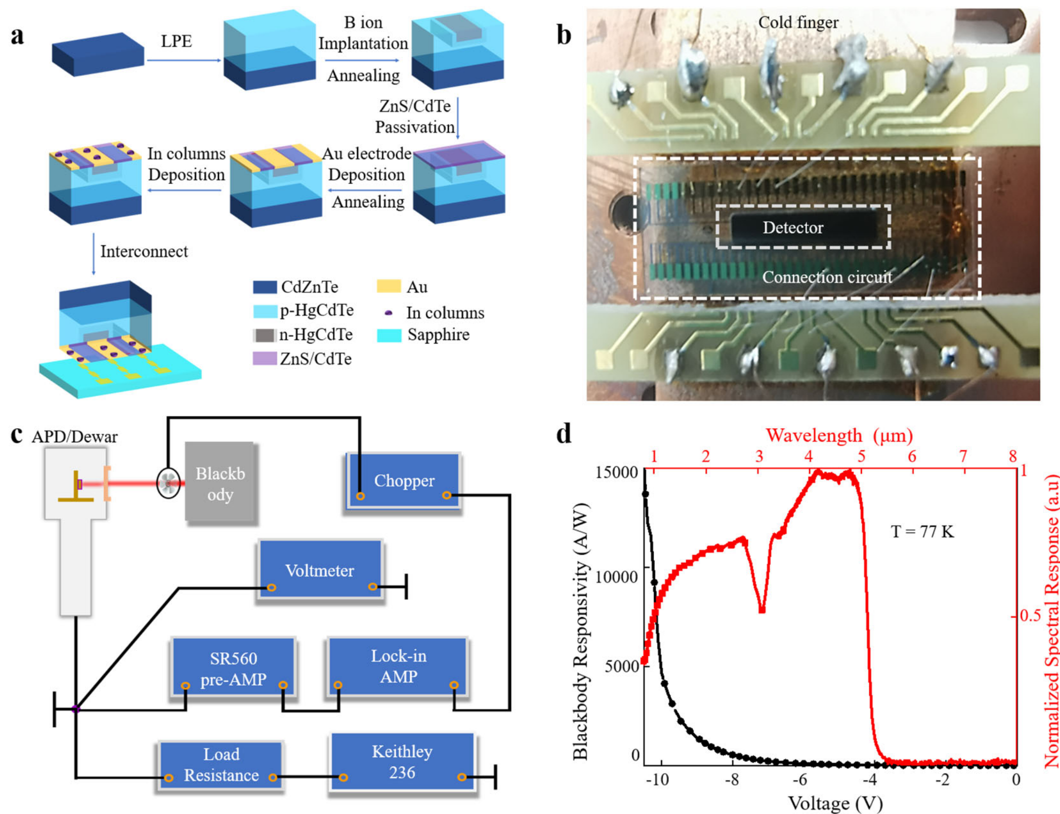

Fig. 4 Fabrication details and the measurement setup. **a** Flow chart of the fabrication process. **b** Optical microscope image of the fabricated HgCdTe APD before measurement. **c** The measurement setup for blackbody responsivity characterization. **d** Measured blackbody responsivity at different reverse bias voltages and the normalized spectral response of our device at 77 K.

in Fig. 4a and a detailed description can be found in the "Methods" section. An optical image of the fabricated HgCdTe avalanche device is shown in Fig. 4b. Conventional measurement setup with current pre-amplifier (SR570, Stanford Inc.) no longer meets the demand of measurement at high reverse bias over 5 V adopted in our previous work[26]. In order to obtain the blackbody responsivity and photocurrent under higher bias, we further implement a voltage amplification characterization system as

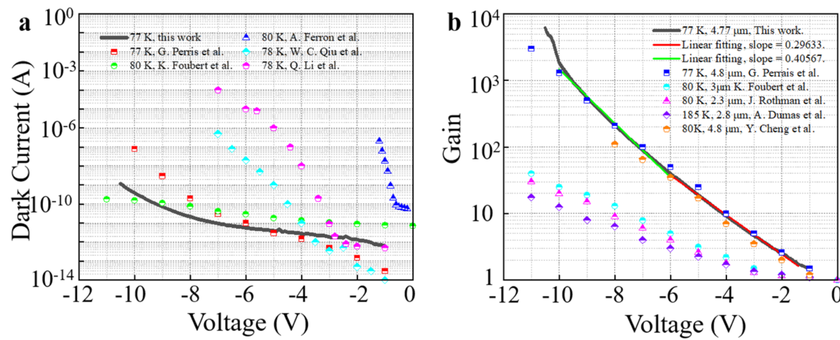

Fig. 5 Key performance of the designed avalanche detector and comparisons with reported devices. a The measured dark current of our own device and the comparisons with others work. **b** The measured avalanche gain of our device and comparisons with others work. Experimental results reported by other groups are included for comparisons.

shown in Fig. 4c. A detailed description of the measurement setup is illustrated in the "Methods" section. As shown in Fig. 4d, the blackbody responsivity illustrates an exponential evolution with increasing the bias voltage, which indicates that a large gain is achieved at a high bias. Besides, the spectral responses of our device and background are measured with a Fourier-transform infrared spectroscope (Nicolet 6700) to calculate the normalized spectral response of the APD in Fig. 4d. It can be seen that the cut-off wavelength of our device is approximately 5 μm. It is worth noting that the dip at about 3 μm is due to the absorptions of carbon dioxide in the atmosphere when capturing the spectrum. The experimental details can be found in Supplementary Note 2. With the normalized spectral response, the g factor is calculated as 5.7018. Together with the blackbody detectivity, D_{bb}^*, the peak photodetectivity D^* is achieved as 2×10^{14} cm Hz$^{1/2}$ W^{-1} at the bias voltage −7.1 V. The calculation details can be found in Supplementary Note 3.

Figure 5a exhibits the experimental results of the dark current of our optimized structure. In order to have a direct evaluation of our device, reported results of single-element devices from other groups are included for comparison. The dark current of our device is 10^{-10}–10^{-9} A under high bias, which in others are larger than 10^{-8} A at high bias[17,19,20,26]. Although the dark current of some devices is slightly lower than ours at lower bias, the gain is lower[27]. Notably, we mainly focus on the device performance under high bias. Since the larger dark current component in our device at high reverse bias is clarified as impact ionization, which is different from cases in reported works, lower overall dark current is achieved with the successful depression of BBT current.

Avalanche gain as another important indicator to characterize the performance of APDs, it can be calculated by $G = [I_{ph}(V) - I_{dark}(V)]/I_{ph}(V = 0) - I_{dark}(V = 0)$ at the certain temperature. Figure 5b shows the experimental results of the avalanche gain as a function of reverse bias. Most of the reported avalanche devices operate in linear mode, whereas the distinction between linear mode and Geiger mode generally corresponds to the sudden change of gain. To avoid potential confusion, here we utilize two linear fittings to illustrate the evolution of the gain curve at different voltage ranges: below –6 V and between −6 and −10 V. The gain reaches 40, 1876, and 6153 at bias −6, −10, and −10.5 V, respectively. We think the voltage node around −10 V is the critical voltage of linear mode and Geiger mode. Remarkably, the gain of our device is much larger than those reported in the literature under high voltage[17,27–30]. Together with the excellent agreements between simulations and experiments, the measured extreme low dark current and high avalanche gain of the optimized device confirm the effectiveness and flexibility in designing high-performance planar PIN HgCdTe APDs.

DISCUSSION

Single-photon detection is the detection limit in the dimension of photon quantity. Considering the unique advantages of MWIR in transmitting through the atmosphere without loss and labeling various materials with spectral fingerprints of molecules based on their characteristic vibrations, efficient and sensitive detection of weak MWIR photons is of great significance in these applications. In this work, we establish a model to clarify the dominating dark current mechanism of the PIN HgCdTe APD at high bias voltages. We find that the ionization avalanche effect and BBT effect both contribute to the overall dark current while the ionization avalanche effect is larger. This breaks the conventional cognition that band-to-band tunneling current prevails in the current competition at high bias. Based on this model with which excellent agreement between simulation and experiment is realized, we optimize the geometric and doping parameters of avalanche structure to achieve high-performance single-photon detectors. With the built voltage amplification characterization setup, we finally achieve gain 1876 (6153) and dark current 10^{-10} (10^{-9}) A @-10 (−10.5) V, respectively. The comparisons with reported works further confirm the superiority of our work. The device we proposed represents a firm step forward towards high-performance photodetectors with extremely low dark current and high avalanche gain. We hope it can do benefit the development of high-performance optoelectronic devices and find applications in ultra-weak photons detection in the relatively immature MWIR regime.

METHODS

Simulation model

The carrier transport is dominated by the drift-diffusion effect and it can be solved by continuity equations with charge conservation. Besides, SRH recombination[31], trap assisted tunneling (TAT)[32], BBT[33], avalanche generation[34], Auger[35], and radiative recombination[36] models are included to perform the numerical calculations. Equations of each model 77 K are listed in Table 1. The corresponding parameters are as follow: $\overrightarrow{J_n}$ and $\overrightarrow{J_p}$ are the electron and hole current density. n and p are the electron and hole density. $R_{net,n}$. and $R_{net,p}$ are the electron and hole net recombination rate, τ_n, and τ_p are the electron and hole lifetime, and E_{trap} is the difference between the defect level and intrinsic level. $a_{n,p}$. is the ionization coefficient, $v_{n,p}$, is the velocity, and A_1, A_7, a and b are all dependent on the temperature T.

Fabrication process

The fabrication process of the optimized structure under our model's guidance is shown in Fig. 4a. P-type HgCdTe material doped by Hg vacancies with a concentration of 8×10^{15} cm^{-3} was grown by the liquid phase epitaxy method, and the Cd component fraction is 0.3. N^+ layer was manufactured with boron (B) ion implantation, and n^- layer was formed via suppressing Hg vacancies in annealing processes. A 200 nm thick ZnS/

Table 1. Current transport models.

Model	Equation
Drift-diffusion model	$\nabla \cdot \overrightarrow{J_n} = qR_{\mathrm{net},n} + q\frac{\partial n}{\partial t}, -\nabla \cdot \overrightarrow{J_p} = qR_{\mathrm{net},p} + q\frac{\partial p}{\partial t}$
SRH recombination & TAT	$R_{\mathrm{net}}^{\mathrm{SRH\&TAT}} = \frac{pn - n_{i,\mathrm{eff}}^2}{\tau_p(n+n_1)+\tau_n(p+p_1)}, n_1 = n_{i,\mathrm{eff}}\exp\left(\frac{E_{\mathrm{trap}}}{kT}\right), p_1 = n_{i,\mathrm{eff}}\exp\left(\frac{-\mathrm{Etrap}}{kT}\right)$
BBT generation	$G^{\mathrm{BBT}} = A_{\mathrm{BBT}}E^P\exp\left(\frac{B_{\mathrm{BBT}}}{E}\right), A_{\mathrm{BBT}} = -\frac{q^2\sqrt{2m_e^*}}{\pi h^2\sqrt{E_g}}, B_{\mathrm{BBT}} = \frac{\pi^2\sqrt{\frac{m_e^*}{2}E_g^{\frac{3}{2}}}}{qh}, P = 2$
Avalanche generation	$G^{\mathrm{Avalanche}} = \alpha_n n v_n + \alpha_p p v_p, \alpha(E) = aE^c\exp\left(\left(-\frac{b}{E}\right)^2\right)$
Auger recombination	$R_{\mathrm{net}}^{\mathrm{Auger}} = A_1 n\left(pn - n_{i,\mathrm{eff}}^2\right) + A_7 p\left(pn - n_{i,\mathrm{eff}}^2\right)$
Radiative recombination	$R_{\mathrm{net}}^{\mathrm{Radiative}} = C\left(pn - n_{i,\mathrm{eff}}^2\right)$

CdTe passivation film was deposited in sequence. Afterward, the Au electrode was deposited after lithography and etching processes, and Ohmic contact was formed after the annealing process. Finally, we deposited the In (indium) bumps for the flip-chip bonding with the readout circuit. The measured doping concentration of n^+ layer and n^- layer is 1×10^{17} and 5×10^{14} cm^{-3}, and the thicknesses of n^+ and n^- layer are 1.5 and 2 μm, respectively. The measured parameters are all included in the simulations.

Measurement setup

Among the voltage amplification measurement setup, the APD is encapsulated in a continuous flow liquid nitrogen Dewar. Keithley 236 is used as a voltage source, and the signal generated in the APD is obtained by the lock-in amplifier after it is amplified by the voltage pre-amplifier (SR560, Stanford Inc.). Here, the load resistance is used to ensure that the alternating current (AC) circuit operates and matches the impedance of the device under test. According to AC equivalence analysis, the photocurrent can be calculated by $I_{\mathrm{ph}} = S/G_{\mathrm{AMP}}/(R_{\mathrm{APD}}//R_{\mathrm{load}})$, in which S is the signals measured by a lock-in amplifier, G_{AMP} is the amplification of SR560 pre-amplifier, and R_{APD} is the dynamic resistance of APD under illumination. The black responsivity can be calculated with $R_{\mathrm{bb}} = I_{\mathrm{ph}}/P_{\mathrm{bb}}$, where P_{bb} is the blackbody power. The radiation power of the blackbody is constant at a fixed operating temperature.

DATA AVAILABILITY

All the raw and derived data that support the findings of this study are available from the authors upon reasonable request.

Received: 10 September 2021; Accepted: 1 December 2021;
Published online: 17 December 2021

REFERENCES

1. Singh, A., Srivastav, V. & Pal, R. HgCdTe avalanche photodiodes: a review. *Opt. Laser Technol.* **43**, 1358–1370 (2011).
2. Rothman, J. Physics and limitations of HgCdTe APDs: a review. *J. Electron. Mater.* **47**, 5657–5665 (2018).
3. Baker, I. M., Finger, G. & Barnes, K. Mercury cadmium telluride focal plane array developments at Selex ES for astronomy and spectroscopy. In *Proc. 40th Conference on Infrared Technology and Applications*. **9070**, 90702U (2014).
4. Sun, X. et al. Evaluation of space radiation effects on HgCdTe avalanche photodiode arrays for lidar applications. *Conf. Infrared Technol. Appl. Xliv* **10624**, 106240G (2018).
5. Rothman, J. et al. HgCdTe APDs detector developments at CEA/Leti for atmospheric lidar and free space optical communications. *Int. Conf. Space Opt.* **11180**, 111803S (2018).
6. Deng, B. et al. Strong mid-infrared photoresponse in small-twist-angle bilayer graphene. *Nat. Photonics* **14**, 549–553 (2020).
7. Rogalski, A. HgCdTe infrared detector material: history, status and outlook. *Rep. Prog. Phys.* **68**, 2267–2336 (2005).
8. Lei, W., Antoszewski, J. & Faraone, L. Progress, challenges, and opportunities for HgCdTe infrared materials and detectors. *Appl. Phys. Rev.* **2**, 041303 (2015).
9. de Lyon, T. et al. Epitaxial growth of HgCdTe 1.55-μm avalanche photodiodes by molecular beam epitaxy. *Optoelectron. '99 -Integr. Optoelectron. Devices* **3629**, 256–267 (1999).
10. Kopytko, M. & Rogalski, A. HgCdTe barrier infrared detectors. *Prog. Quantum Electron.* **47**, 1–18 (2016).
11. Senanayake, P. et al. Thin 3D multiplication regions in plasmonically enhanced nanopillar avalanche detectors. *Nano Lett.* **12**, 6448–6452 (2012).
12. Zhao, X., Jiang, D., Zhao, M. & Duan, Y. Avalanche effect and high external quantum efficiency in MgZnO/Au/ZnO sandwich structure photodetector. *Adv. Opt. Mater.* **9**, 2002023 (2021).
13. Bulgarini, G. et al. Avalanche amplification of a single exciton in a semiconductor nanowire. *Nat. Photonics* **6**, 455–458 (2012).
14. Hadfield, R. H. Single-photon detectors for optical quantum information applications. *Nat. Photonics* **3**, 696–705 (2009).
15. Dam, J. S., Tidemand-Lichtenberg, P. & Pedersen, C. Room-temperature mid-infrared single-photon spectral imaging. *Nat. Photonics* **6**, 788–793 (2012).
16. Gibson, S. J. et al. Tapered InP nanowire arrays for efficient broadband high-speed single-photon detection. *Nat. Nanotechnol.* **14**, 473–479 (2019).
17. Perrais, G., Rothman, J., Destefanis, G. & Chamonal, J.-P. Impulse response time measurements in Hg0.7Cd0.3Te MWIR avalanche photodiodes. *J. Electron. Mater.* **37**, 1261–1273 (2008).
18. Singh, A., Shukla, A. K. & Pal, R. High performance of midwave infrared HgCdTe e-avalanche photodiode detector. *IEEE Electr Device L* **36**, 360–362 (2015).
19. Qiu, W.-C. et al. Dark current transport and avalanche mechanism in HgCdTe electron-avalanche photodiodes. *IEEE T. Electron Dev.* **62**, 1926–1931 (2015).
20. Li, Q. et al. Influencing sources for dark current transport and avalanche mechanisms in planar and mesa HgCdTe p-i-n electron-avalanche photodiodes. *IEEE T. Electron Dev.* **65**, 572–576 (2018).
21. He, J. et al. Design of a bandgap-engineered barrier-blocking HOT HgCdTe long-wavelength infrared avalanche photodiode. *Opt. Express* **28**, 33556–33563 (2020).
22. Hu, W. et al. Accurate simulation of temperature-dependent dark current in HgCdTe infrared detectors assisted by analytical modeling. *J. Electron. Mater.* **39**, 981–985 (2010).
23. Kopytko, M. et al. Impact ionization in HgCdTe avalanche photodiode optimized to 8 μm cut-off wavelength at 230 K. *Infrared Phys. Techn.* **115**, 103704 (2021).
24. Li, Q. et al. Enhanced performance of HgCdTe midwavelength infrared electron avalanche photodetectors with guard ring designs. *IEEE T. Electron Dev.* **67**, 542–546 (2020).
25. Chen, J. et al. Uniformly broadband far-infrared response from the photocarrier tunneling of mesa Si:P blocked-impurity-band detector. *IEEE T. Electron Dev.* **68**, 560–564 (2021).
26. Ferron, A., Rothman, J. & Gravrand, O. Modeling of dark current in HgCdTe infrared detectors. *J. Electron. Mater.* **42**, 3303–3308 (2013).
27. Foubert, K. et al. Development of HgCdTe single-element APDs based detectors for low flux short wave infrared applications. *Conf. Opt. Compon. Mater. X.* **8621**, 86210F (2013).
28. Dumas, A. et al. Evaluation of a HgCdTe e-APD based detector for 2 μm CO2 DIAL application. *Appl. Opt.* **56**, 7577–7585 (2017).
29. Cheng, Y. et al. Improved local field model for HgCdTe electron avalanche photodiode. *Infrared Phys. Techn.* **101**, 156–161 (2019).
30. Rothman, J., Foubert, K., Lasfargues, G. & Largeron, C. Response time measurements in short-wave infrared HgCdTe e-APDs. *J. Electron. Mater.* **43**, 2947–2954 (2014).
31. Tyagi, M. S. & Vanoverstraeten, R. Minority-carrier recombination in heavily-doped silicon. *Solid State Electron.* **26**, 577–597 (1983).
32. Nemirovsky, Y., Fastow, R., Meyassed, M. & Unikovsky, A. Trapping effects in HgCdTe. *J. Vac. Sci. Technol. B* **9**, 1829–1839 (1991).

33. Anderson, W. W. Tunnel current limitations of narrow bandgap IR charge coupled devices. *Infrared Phys.* **17**, 147–164 (1977).
34. Okuto, Y. & Crowell, C. R. Threshold energy effect on avalanche breakdown voltage in semiconductor junctions. *Solid State Electron.* **18**, 161–168 (1975).
35. Beattie, A. R. & Landsberg, P. T. Auger effect in semiconductors. *Proc. R. Soc. Lond. Ser. A* **249**, 16–29 (1959).
36. Vanroosbroeck, W. & Shockley, W. Photon-radiative recombination of electrons and holes in germanium. *Phys. Rev.* **94**, 1558–1560 (1954).

ACKNOWLEDGEMENTS

This work was supported in part by the National Key Research and Development Program of China under Grant 2018YFA0306200 and Grant 2017YFA0205800; in part by the National Natural Science Foundation of China under Grant 61875218, Grant 61521005, Grant 61991440, and Grant 91850208; in part by the Youth Innovation Promotion Association of Chinese Academy of Sciences under Grant 2017285; in part by the Key Research Project of Frontier Science of Chinese Academy of Sciences under Grant QYZDJSSWJSC007; in part by the Strategic Priority Research Program of Chinese Academy of Sciences under Grant XDB43010200; in part by the Shanghai Rising-Star Program under Grant 20QA1410400; in part by the Shanghai Science and Technology Committee under Grant 18JC1420401 and Grant 20JC1416000; in part by the Zhejiang Provincial Natural Science Foundation under Grant LR22F050004, and in part by the Shanghai Municipal Science and Technology Major Project under Grant 2019SHZDZX01. This work was partially carried out at the Center for Micro and Nanoscale Research and Fabrication at the University of Science and Technology of China.

AUTHOR CONTRIBUTIONS

Jin Chen, Jian Chen and Xin Li contribute equally. Guanhai Li conceived the original ideas presented in this work. Jin Chen, Jian Chen and Jian Wang setup the measurement system and measured these devices. Liao Yang, Chuan Shen and Huijun Guo fabricated these devices. Xin Li, Jian Chen and Jiale He carried out the numerical simulations. Guanhai Li, Xiaoshuang Chen and Wei Lu analyzed the data and discussed the results. Feilong Yu and Zengyue Zhao guided the measurement. The manuscript was jointly written by Guanhai Li, Jin Chen and Jian Chen. Guanhai Li and Xiaoshuang Chen organized the project, analyzed the results, and prepare the manuscripts. All authors discussed the results and commented on the manuscript.

COMPETING INTERESTS

The authors declare no competing interests.

ADDITIONAL INFORMATION

Supplementary information The online version contains supplementary material available at https://doi.org/10.1038/s41535-021-00409-3.

Correspondence and requests for materials should be addressed to Guanhai Li.

Reprints and permission information is available at http://www.nature.com/reprints

Publisher's note Springer Nature remains neutral with regard to jurisdictional claims in published maps and institutional affiliations.

Open Access This article is licensed under a Creative Commons Attribution 4.0 International License, which permits use, sharing, adaptation, distribution and reproduction in any medium or format, as long as you give appropriate credit to the original author(s) and the source, provide a link to the Creative Commons license, and indicate if changes were made. The images or other third party material in this article are included in the article's Creative Commons license, unless indicated otherwise in a credit line to the material. If material is not included in the article's Creative Commons license and your intended use is not permitted by statutory regulation or exceeds the permitted use, you will need to obtain permission directly from the copyright holder. To view a copy of this license, visit http://creativecommons.org/licenses/by/4.0/.

© The Author(s) 2021